Ultrathin Bioelectrode Array with Improved Electrochemical Performance for Electrophysiological Sensing and Modulation

Abstract

Sensing and modulating neural activities with high efficacy and accuracy depend on stable, effective, and spatiotemporally precise biointerfaces. Thin bioelectronics offer mechanical compliance by forming seamless contact with biological tissues. Nevertheless, achieving reliable electrochemical performance in thin bioelectronics remains challenging. Here, we report an ultrathin (~ 115 nm), multi-channel bioelectrode array that simultaneously enables ultra-conformability and high electrochemical performance. It shows high optoelectrical conductivity (2060 S cm^{-1} @ 88% transparency), mechanical stretchability (110% strain), and excellent electrochemical performance (24.5 mC cm^{-2} charge storage capacity, 3.5 times lower interfacial impedance than commercial electrode). The enhanced mechano-electrical and electrochemical performance is attributed to the synergistic interactions within poly (3,4-ethylenedioxythiophene): polystyrene sulfonate (PEDOT:PSS) / graphene oxide (GO) interpenetrating network (PGIN). These interactions, including π-π interaction and hydrogen bonding, not only modify the structure of PEDOT to a more linear arrangement but also enhance charge transfer mobility. The ultra-thin bioelectrode array demonstrates exceptional capability in sensing and modulating neuromuscular activities with high fidelity. By further applying PGIN bioelectrode array to accurately capture weak facial electromyography signals, and performing machine learning algorithms, we have achieved high accuracy in silent speech recognition. This ultra-conformal bioelectrode array shows great promise in health management and human-machine interface.

Introduction

Sensing and modulating neutral activities are of particular importance in health monitoring, clinical treatment, human-machine interaction, and other applications[1-3].[1-3] For example, electromyography (EMG) measures the electrical activity of skeletal

muscles by sensing the variations in biopotential within muscle cells. By integrating EMG with machine learning algorithms, its application extends to areas such as muscle fatigue prediction and prosthetic control[4-7].[4-7] Moreover, simultaneous provision of feedback, which is instrumental in modulating excitable cells is crucial for the restoration of muscle function[8,9].[8,9] Such bidirectional communication between human tissues and bioelectronics highly relies on reliable and effective senor-biotissue interfaces, which require the bioelectrodes to form intimate contact with curvilinear tissue surfaces and have excellent electrochemical properties[10-13].[10-13] Additionally, a higher spatial resolution is required for a more detailed and accurate mapping of biological signals[14,15].[14,15]

Poly(3,4-ethylenedioxythiophene):poly(styrene sulfonate) (PEDOT:PSS), a mature commercial conductive polymer, stands out as an ideal bio-interfacing material for its solution processability, mixed ionic and electronic conductivity and biocompatibility[18,19].[18,19] However, the intrinsic conductivity of PEDOT: PSS is limited (~ 0.1 S cm^{-1}), and the inherent mechanical property is not sufficient to match biological tissues (~ 5% strain at break), which can affect the efficacy and stability of signal transmission[20,21].[20,21] To enhance the conductivity and stretchability of PEDOT: PSS, various strategies have been developed, including the addition of ionic liquids and surfactants, as well as blending with plasticizers and polymers[22-24].[22-24] While these approaches can enhance the electrical and mechanical properties of PEDOT:PSS to a degree, they come with drawbacks such as risk of ionic liquid leakage, and tradeoff between conductivity and stretchability. Apart from this, there is a growing demand for multi-channel electrodes to facilitate detailed information mapping. Efforts to pattern PEDOT: PSS have utilized various methods, such as screen printing, inkjet printing, laser-induced digital patterning, and photolithography through blending with ultra-violet (UV) sensitive polymers[25-30].[25-30] However, printing technology is hard to achieve uniform film thickness and consistency, while laser-induced digital patterning and photolithography do not typically produce PEDOT:PSS films with high conductivity or the materials synthesis is sophisticated. Therefore, patterning

PEDOT:PSS with excellent electrical and electrochemical properties, and suitable mechanical mismatch to biological tissues in a simplifying fabrication way is in urgent need.

Effective and stable biointerfaces, which feature excellent electrochemical properties and seamless contact with human tissues, are crucial in electrophysiological sensing and modulating. Graphene is attractive in this domain due to its excellent electrical property, chemical stability, mechanical flexibility, and mechanical robustness[31,32].[31,32] Researches have shown that combining PEDOT:PSS with graphene enhances the stability of bioelectrodes and reduces their interfacial impedance[33,34].[33,34] However, the electrochemical performance of single layer graphene is inferior to graphene oxide (GO), primarily due to its limited surface to volume ratio[35].[35] Additionally, the use of PEDOT:PSS/GO composite as coating layers, which typically results in substantial thicknesses, presents challenges in forming conformal contact with uneven tissue surface, as the film's bending stiffness increases exponentially with its thickness[36].[36] Therefore, fabricating thin PEDOT: PSS/GO bioelectrodes in conjunction with photolithographic technology, may develop multi-channel bioelectrode array with low interfacial impedance, high charge storage capacity, and compliance to biological tissues.

Here, we developed an ultra-conformal and multi-channel bioelectrode array enabled by PEDOT:PSS/GO interpenetrating network (PGIN) for high-performance electrophysiological sensing and modulating. The fabrication of PGIN involves mixing and photopatterning of a mixture containing conductive polymer (PEDOT:PSS) and GO crosslinked by polyethylene glycol dimethacrylate (PEGDMA) (Fig. 1a). This unique formulation endows PGIN films with exceptional properties: opto-electrical conductivity of 2060 S cm^{-1} @ 88% transparency, a mechanical stretchability of up to 110% strain, excellent electrochemical performance and design flexibility. Significantly, the electrochemical enhancements of PGIN can be attributed to two key factors: (i) a reduced interfacial impedance owing to high charge transfer efficiency and superior

conformability with biological tissues; (ii) a strengthened charge storage capacity, bolstered by the GO's high surface-to-volume ratio. Furthermore, the intricate interactions within PGIN including π-π and hydrogen bonding interactions were systematically studied, showcasing the depth of engineering at the molecular level. PGIN also excels in multi-channel electrophysiological sensing and modulating. When integrated with machine learning algorithms, PGIN achieves high accuracy in silent speech recognition. By developing this ultra-conformal and solution-processable multi-channel bioelectrode array, we provide valuable insights into the construction of efficient and stable biointerfaces, thereby streamlining the pathway towards innovative biomedical researches.

Result

Design and fabrication of PGIN

To date, the approaches to achieve direct photolithography of conductive polymers are to blend them with cross-linkers or functional polymers. However, the synthesis conditions for functional polymers are harsh and complicated, and the additional polymers can compromise the opto-electrical properties of electrodes. To develop a more accessible approach while marinating high opto-electrical conductivity, mechanical stretchability, and design versatility, we rationally designed an interpenetrating network composed of conductive polymer (PEDOT:PSS), GO, and UV-sensitive crosslinker. The molecular structure of PEODT:PSS and GO both include benzene rings, which facilitate potential π-π conjugation interactions, leading to improved charge transfer efficiency (Fig. 1a). This conductive film was fabricated by following steps: i) mixing the components into homogeneous aqueous precursor; ii) spin-coating the precursor on substrate; iii) patterning the precursor by forming the PEDOT: PSS/GO interpenetrating network (PGIN).

In general, the interactions of polymer chains in PGIN are mainly: i) π-π interactions between PEDOT and GO; ii) hydrogen bonds interaction between PSS and GO; iii)

hydrogen bonds interaction between PSS and PEG (Fig.1b). The multiple interactions in PGIN contribute to the alignment of PEDOT, facilitating its transition from a coil structure to a more extended structure. Such a transition is conducive to the formation of a continuous conductive network for enhancement of electrical conductivity. Atomic force microscope (AFM) phase images confirmed the formation of an interconnected nanofibrillar structure facilitated by the synergistic interactions between PEDOT:PSS and GO. Specifically, the charge transfer mechanism was analyzed by theoretical calculation (Fig. 1f). The charge difference between PEDOT and GO, where the yellow regions express electron aggregation and the blue regions express electron deficiency, indicates the electrons transmitted from GO to PEDOT through π-π interaction. The establishment of an electron path further improves the electrical conductivity of PGIN. Additionally, GO introduces more active sites for ions trapping and de-trapping, endowing the ultra-conformal electrode a relatively higher capacitance. Together with the high electrical conductivity, as-fabricated ultraconformal electrodes will result in a low electrochemical impedance. Credit to its compatibility with photolithography, PGIN can be customized into various patterns to meet the diverse requirements of bioelectronics. The ultrathin multi-channel shaped PGIN tattoo film adhered to the wrist demonstrating ultra-conformability, which is essential for achieving low interfacial impedance (Fig. 1e). Overall, the PGIN film, prepared through solution processing, exhibits ultra-conformality, low electrochemical impedance, and adaptability in design, making it an ideal interface for electrophysiological sensing and modulation (Supplementary Fig. S1).

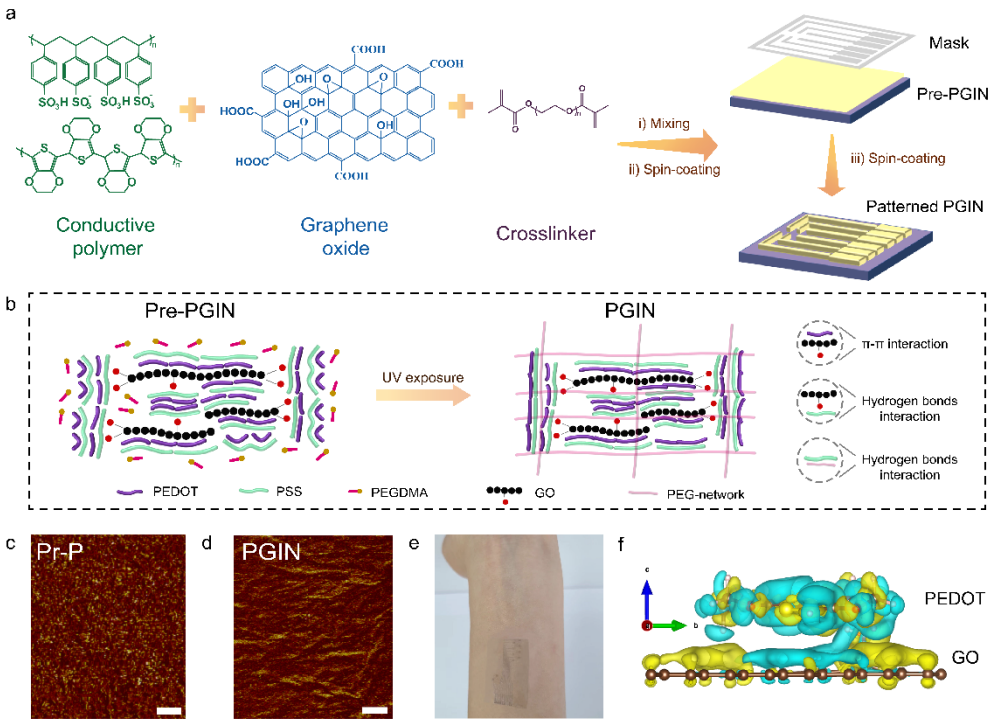

Fig. 1 Fabrication of an ultrathin and patternable PGIN film with a low electrochemical impedance. a Schematic illustration of the fabrication process of PGIN, and chemical structure of PEDOT:PSS, GO, and PEGDMA. **b** Schematic diagram illustrating the patterning mechanism and multiple interactions in PGIN film. Pre-PGIN denotes uncrosslinked PEDOT:PSS/GO/PEGDMA. **c, d** Comparison of AFM phase images of pristine PEDOT:PSS (Pr-P) and PGIN, showing the nanofibrillar structure induced by GO. Scale bar, 0.5 μm. **e** A photo showing PGIN electrode array on tattoo conformably adhered to a hand. **f** Charge density difference for the interfaces between PEDOT and GO, showing the charge transfer between PEDOT and GO. The yellow regions express electron aggregation and the blue regions express electron deficiency.

Mechano-electrical performance of PGIN

Although PEDOT:PSS is intrinsically conductive, the electrically conductivity of pristine PEDOT: PSS (Pr-P) film is very low (~ 0.1 S cm^{-1}), which is insufficient for application as a bioelectrode. We first investigated the synergistic effect of GO on the electrical property of PGIN. Due to the components' high solubility in water, uniform

films can be prepared through the spin-coating technique. The conductivity of PGIN films with various GO wt% loading were characterized (Fig. 2a). Interestingly, with the increased loading of the insulating GO, the conductivity of PGIN film was improved by as many as 33 times. We infer the enhancement of conductivity is due to the synergistic interactions between PEDOT:PSS and GO. GO is characterized by a rich functional group on its surface, including hydroxyl (-OH) and carboxyl (-COOH) groups, which can be seen as negatively charged. Concurrently, PEDOT and PSS are bound together through Coulomb (electrostatic) interaction, where PEDOT is positively charged and PSS is negatively charged. When these two materials are mixed in a system, the negatively charged GO can attract the positively charged PEDOT segments, resulting in a close association between GO and PEDOT:PSS. Given the structural similarity of PEDOT and GO in π-conjugated networks, they can engage in π-π interactions, thereby enhancing the electronic communication within the film. In addition, hydroxyl groups on GO can form hydrogen bonds with the sulfonate groups ($-SO_3^-$) on PSS, causing partial phase separation between PEDOT and PSS, contributing to the improved conductivity. To further enhance the conductivity, PGIN film was post-treated with sulfuric acid (termed as PGIN-S). By removing excess PSS, PGIN-S can achieve a conductivity as high as 2060 S cm^{-1} with 7 wt% GO loading (Fig. 2b). Note that when GO loading reached 10 wt%, the conductivity of PGIN-S film decreased, which may be due to the nonuniformity caused by aggregation of GO. Moreover, the transmittance of PGIN-S films decreased with the loading of GO, but still maintained over 85% (Supplementary Fig. S2).

Then, the colloidal charge of components in water was studied. When GO was introduced to a mixture of PEDOT: PSS/PEGDMA, a notable decrease in zeta potential was observed, dropping to approximately -35.8 eV with a GO loading of 7 wt%. This reduction signifies the formation of a more stable colloidal system. However, with the GO loading increased to 10 wt%, the zeta potential increased to ~ -32.5 eV, which may be owing to the aggregation tendency of GO. Thus, a 7 wt% GO loading is optimal for achieving a uniform PGIN film. Additionally, the impact of PEGDMA presence on the

zeta potential was assessed by comparing solutions with and without this component. The inclusion of PEGDMA resulted in a lower zeta potential, thereby underscoring its role in enhancing solution stability (Supplementary Fig. S3). To observe the morphology and structure of PGIN, transmission electron microscopy (TEM) was conducted. For Pr-P, the composition included nanoparticles varying in size from 20 to 50 nm, demonstrating their good dispersity. The single-layer GO sheet typically exhibited a wrinkled structure with a size of ~ 1 μm, showing its thin nature and mechanical flexibility (Supplementary Fig. S4). Then, PGIN solution was diluted and sonicated for scanning transmission electron microscopic-energy dispersive spectroscopy (STEM-EDS) mapping to observe the distribution of elements. The result showed that sulfur atoms were anchored on the surface of GO, suggesting a strong interaction between GO and PEDOT: PSS (Fig. 2d).

Next, the mechano-electrical property of PGIN was investigated. PGIN-S films with various GO concentrations were fabricated on elastomeric styrene-ethylene-butadiene-styrene (SEBS) substrates. By applying strains on SEBS substrates, PGIN with 7 wt% GO loading (7% PGIN-S) showed better mechano-electrical property (110% strain) (Fig. 2e). The results suggested that the synergistic interaction between GO and PEDOT: PSS enhanced the mechanical stretchability of PGIN, and the uniformity of the film was also important for optimizing the performance. During the mechanical durability test, 7% PGIN-S demonstrated stable resistance change, maintaining its performance through 2000 cycles under 30% strain. Therefore, the optimal composition for PGIN was selected as 7 wt% loading of GO and post-treated with sulfuric acid.

To understand the enhanced mechano-electrical stability in PGIN films, AFM imaging was utilized to examine various PEDOT:PSS films (Fig.2g). Upon applying a 30% strain to SEBS substrate, large cracks, mostly perpendicular to the strain direction, were observed in Pr-P. With the formation of PEDOT:PSS/PEG interpenetrating network (PPIN), the crack became smaller, likely due to the weakened Coulomb attraction between PEDOT and PSS, which facilitated the slippage of the polymer chains. After

introducing GO into the interpenetrating network, the crack almost disappeared. This change suggests that the synergistic interaction between GO and PEDOT: PSS, along with the mechanical flexibility of GO sheets, improved the film's resistance to crack propagation. Generally, the multiple interactions between PEDOT:PSS and GO contribute to the enhancement of mechano-electrical stability of the PGIN film.

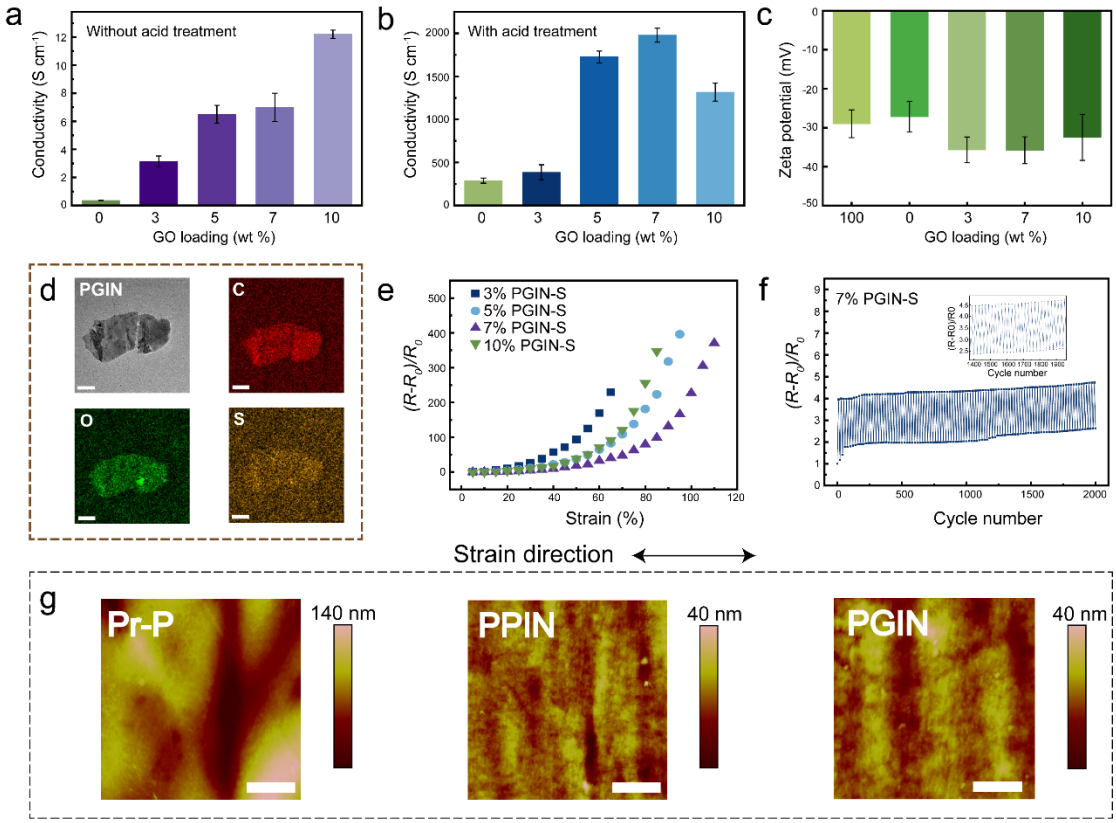

Fig. 2 Mechano-electrical performance of PGIN. a, b Conductivity comparison of PGIN before (**a**) and after (**b**) sulfuric acid post-treatment for various GO loadings from 0 to 10 wt%. **c** Zeta potential of different mixed dispersions. **d** TEM image of a diluted PGIN mixture alongside STEM-EDS mapping for carbon (C), oxygen (O), and sulfur (S), demonstrating the aggregation of sulfur on a GO flake. Scale bar, 100 nm. **e** Normalized resistance changes of PGIN-S with 3-10 wt % GO loading. **f** Normalized resistance change of PGIN under cyclic strain (30%) loading. **g** AFM images of Pr-P, PPIN and PGIN upon 30% strain. Scale bar, 1 μm.

Synergistic interactions between polymer chains and GO

To explore the synergistic interactions between polymer chains and GO, we undertook a thorough investigation into the structure of PGIN. Grazing-incidence wide-angle X-ray scattering (GIWAXS) serves as an advanced method for analyzing the structure of thin films and determining the alignment of polymer crystallites [37,38].[37,38] 2D GIWAXS patterns were compared between Pr-P, PPIN, PGIN, and PGIN-S films (Fig. 2a, Supplementary Fig. S5). The π–π stacking distance of PEDOT along the in-plane direction was calculated from (010) peak at around q_z = 1.8 $Å^{-1}$ through Bragg's law. For various PEDOT films, the π–π stacking distances are 3.65 Å (Pr-P), 3.48 Å (PPIN), 3.31 Å (PGIN), and 3.33 Å (PGIN-S) (Fig. 3c). With the addition of PEGDMA and GO, the π-π stacking distance continually decreased, indicating a more compact and ordered structure of PEDOT chains. Notably, the π–π stacking distance reached an extremely small value compared to reported PEDOT: PSS/graphene film[33].[33] This is attributed to the improved interaction between GO and PEDOT: PSS in solution, as opposed to the graphene film grown by chemical vapor deposition (CVD) method. AFM imaging was subsequently carried out to assess the morphological changes in various PEDOT films (Fig. 3b, Supplementary Fig. S6). Compared to Pr-P, PGIN exhibited noticeable interconnected fibrils, resulting in a 5.5-fold increase in roughness (Fig. 3c). This roughness was further amplified by acid treatment, which facilitated phase separation between PEDOT and PSS through the removal of PSS. The observed microstructural alterations suggested a more orderly arrangement and crystallization of PEDOT. Such changes are indicative of an enhanced charge transfer efficiency, demonstrating how PEGDMA, GO and acid treatment can synergistically modify the electrical property of PEDOT films.

X-ray photoelectron spectroscopy (XPS) revealed a decreasing trend of PSS/PEDOT ratio with the addition of PEGDMA and GO. This decrease indicated the removal of the insulating PSS, likely due to the formation of hydrogen bonds with PSS (Fig. 3e). Furthermore, a higher concentration of GO resulted in a lower PSS/PEDOT ratio, which can be attributed to the increased number of functional groups on GO, facilitating the

interaction with PSS (Supplementary Fig. S7). The post-treatment with acid significantly reduced the PSS and increased the proportion of PEDOT, further improving the packing of PEDOT chains. Fourier transform infrared spectroscopy (FTIR) was conducted to understand the interaction between PEDOT: PSS and GO. GO exhibited infrared absorption at 1693 cm^{-1}, indicative of C=O stretching and vibrations. After its incorporation into PPIN, the absorption wavenumber shifted to 1690 cm^{-1}. This shift from 1693 cm^{-1} to 1690 cm^{-1} suggested the formation of hydrogen bonds between GO and the PEDOT: PSS/PEGDMA composite. Raman spectroscopy was used to probe the structural transformation of PEDOT chains by analyzing the peak at ~ 1430.0 cm^{-1}, which corresponds to symmetric C_α=C_β stretching vibrations of the thiophene ring of PEDOT. Blending with PEGDMA induced a blue shift of this peak to 1440.6 cm^{-1}, which confirmed a strong interchain coupling between the polymer chains. After introducing GO, the peak red shifted to 1434.1 cm^{-1}, indicating a structural transformation from benzoid/coil to quinoid/linear through π-π interaction. Given that the linear structure is more favorable for charge transfer between PEDOT chains, the addition of GO can increase the charge carrier mobility within PGIN, thus enhance the conductivity of PGIN film (Supplementary Fig. S8). Post-treatment with acid positively affected the transformation to a more extended structure. Apart from this, ultraviolet-visible-near infrared (UV-vis-NIR) and electron spin resonance (ESR) spectroscopies were used to analyze the π-conjunction structures and π-delocalization degrees of various PEDOT films. The presence of a broad peak at ~ 800 nm in UV-vis-NIR spectroscopy suggested a high degree of π-π transition, associated with the extended conjugation length of PEDOT chains (Supplementary Fig. S9). Apart from this, a significant decrease in absorption peak was observed in PGIN, which was indicative of enhanced electronic interactions between PEDOT and GO, and the charge carriers' transition from polarons to bipolarons (Fig. 3h). Such transition facilitated a more efficient charge transport along the polymer chains, leading to higher conductivity.

On the whole, the synergistic interactions within PGIN can be concluded as: i) GO modifies the structure of PEDOT chains by inducing a more extended configuration

and dense packing via π-π interaction; ii) functional groups on GO such as hydroxyl and carboxyl groups form hydrogen bonds with PSS. This interaction serves a dual role: it induced phase separation between PEDOT and PSS, while simultaneously facilitating the alignment of the PEDOT chains for interconnected conductive network; iii) PEGDMA increases the crystallinity of PEDOT through hydrogen bonding with PSS; iv) post-treatment with acid removes excess insulating PSS. The above interactions all contributed to the enhancement of electrical pathways and charge transfer efficiency, leading to excellent mechano-electrical performance of PGIN.

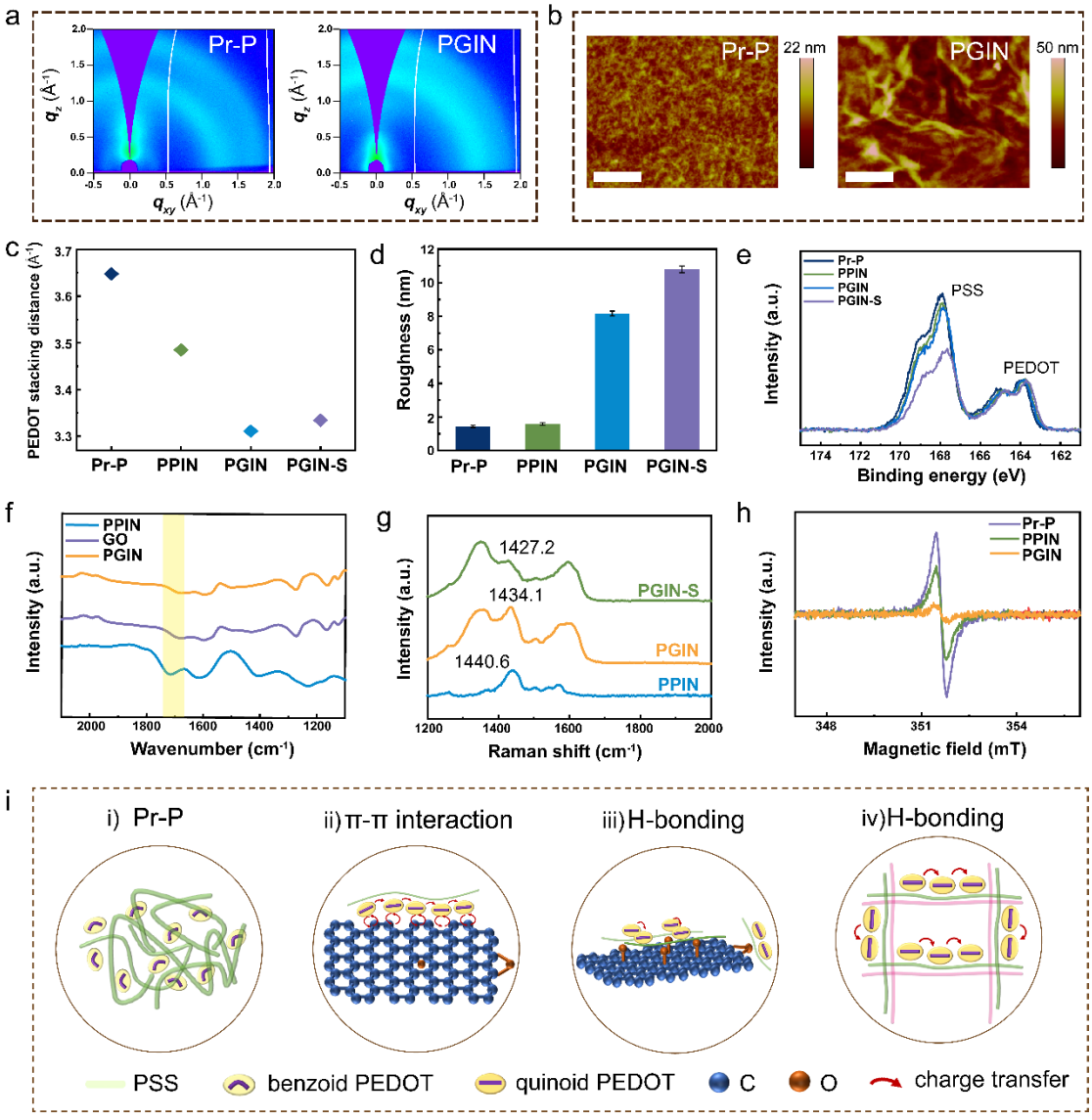

Fig. 3 Synergistic interactions between polymer chains and GO. a 2D GIWAXS

patterns of Pr-P and PGIN. **b** AFM images of Pr-P and PGIN. Scale bar, 1 μm. **c** Comparison of PEDOT π-π stacking distances of various PEDOT films. **d** Comparison of roughness of various PEDOT films. **e** XPS spectra (S_{2p}) of various PEDOT films. The sulfur peaks (S_{2p}) of PEDOT thiophene (166 -162 eV) were normalized. **f** FTIR spectra of PPIN, GO, and PGIN. **g** Raman spectra of PPIN, PGIN and PGIN-S. **h** ESR spectra of Pr-P, PPIN and PGIN. **i** Schematic illustration of the synergistic interactions in PGIN. Compared to Pr-P (**a**), the addition of GO and PEGDMA induced π-π (**b**) and hydrogen bonds interactions (**c, d**).

Mechanism of synergistic interactions in PGIN

To deepen our understanding of the synergistic interaction mechanisms within PGIN, we carried out density functional theory (DFT) calculations to explore the binding energy between polymer chains and GO, as well as the charge distribution between GO and PEDOT. Firstly, we investigated the interaction between PEDOT: PSS and GO. The binding energy between GO and PEDOT is -6.89 eV, indicating a strong affinity between negatively charged GO and positively charged PEDOT (Fig. 4a). This affinity is primarily facilitated by the π-π interaction between PEDOT and GO, which lead to a notable reduction in the π-π distances within the PEDOT chains. Moreover, the binding energy between GO and PSS was calculated as -6.63 eV, confirming the formation of hydrogen bonds between GO and PSS (Fig. 4b). The hydrogen bonding between PSS and PEG was also verified by DFT calculations (Supplementary Fig. S10). Furthermore, our studies revealed an binding energy between GO and PEG was -5.61 eV, indicating the occurrence of hydrogen bonding (Supplementary Fig. S11).

Subsequently, we employed the electron localization function to examine the charge distribution within PGIN (Fig. 3c). The incorporation of GO led to a higher density of state (DOS) at the Fermi level compared to PEDOT only (Fig.3d). This elevation suggests improved electronic properties, including enhanced electrical conductivity and electrochemical performance. Such improvements are attributed to the introduction of new electronic states by GO and the alteration in the alignment of energy levels between

GO and PEDOT, which collectively amplify the density of states available for conduction. To elucidate the mechanism of charge transfer between GO and PEDOT, the difference in charge density was analyzed, with yellow denoting areas of electron aggregation and blue denoting areas of electron deficiency (Fig. 3e). The observations confirmed facilitation of electron transport between GO and PEDOT, indicating the role of GO in providing effective pathways for enhancing the material's overall conductivity. The above theoretical analysis not only illuminates the pivotal role of GO in augmenting the electronic properties of PGIN but also substantiates its efficacy in serving as a bridge for charge transfer, which is beneficial for the electronic and electrochemical applications of PGIN.

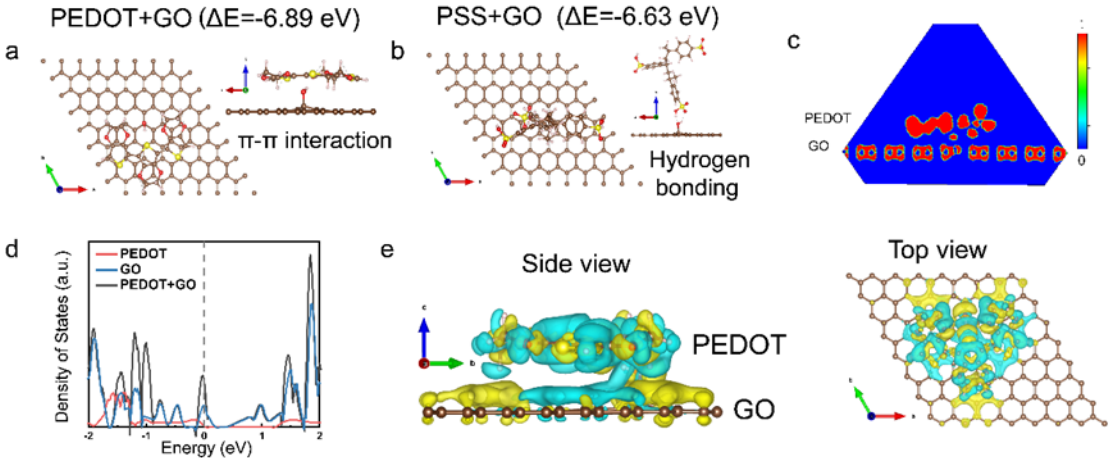

Fig. 4 Mechanism of synergistic interactions in PGIN. a Optimized structure of the modelled PEDOT+GO (Top view). The inset is the side view. **b** Optimized structure of the modelled PSS+GO (Top view). The inset is the side view. **c** The electron localization function of PEDOT+GO. **d** The total density of state (DOS) of PEDOT and PEDOT+GO, indicating charge transfer between PEDOT and GO through π-π interaction. **e** Side and top views of charge density difference for the interfaces between PEDOT and GO. The yellow regions indicate electron aggregation and the blue regions indicate electron deficiency. Carbon atoms are brown, oxygen red, sulfur yellow, and hydrogen white.

Electrophysiological sensing and modulating of PGIN bioelectrode

Electrophysiological sensing and modulation serve as pivotal methodologies in diagnosing and treating nervous system disorders by recording and manipulating neuronal activities. To achieve a stable and effective bidirectional neutral interface, it is critical to ensure excellent electrochemical performance, including low interfacial impedance and high charge transfer capacity. Consequently, the construction of an intimate interface between biological tissues and electrodes is essential, as the existence of air gaps can increase the interfacial impedance, thereby degrading the quality of signal (Fig. 5a). To evaluate the electrochemical performance of PGIN electrode, we conducted impedance analysis using a pair of PGIN electrodes placed on the human arm. Compared to commercial Ag/AgCl and Pr-P electrodes, PGIN showed much lower impedance at both 10 and 100 Hz. This indicates that PGIN electrode achieved a conformable adherence to skin owing to its ultrathin nature, while also showing its superior electrical property. In addition, attributed to the high aspect ratio of GO, PGIN demonstrated an enhanced charge storage capacity per unit area (24.5 mC cm^{-2}) over Pr-P (5.0 mC cm^{-2}) (Fig.5d). The nearly five-fold increase indicates that GO contributes additional active sites for charge storage, thus enhancing the effective surface area of PGIN. Leveraging this enhanced capability, we deployed PGIN for neuromuscular electrical modulation. The PGIN electrode was conformably adhered on the hand, targeting accurate trigger points related to brachial plexus (Fig. 5e), while a six-channel PGIN electrode array was adhered on the arm as a recording electrode to capture the evokes response (denoted as S: PGIN, R: PGIN). In comparison with Ag/AgCl electrode, PGIN exhibited stronger electrostimulation capability at identical frequency and voltage amplitude (2 Hz, 2 V), showcasing its superiority in neuromodulation efficacy (Fig. 5g, h). Furthermore, when utilized six-channel Ag/AgCl electrodes to capture the evokes response, there was a noticeable degradation in signal quality (Fig. 5f). This deterioration can be linked to the inability of the Ag/AgCl electrodes to conform effectively to the skin.

Given that the human body is frequently in motion, the performance of bioelectrodes under motion becomes crucial. To evaluate the recording capability of PGIN in motion,

an electrical vibrator was placed near a pair of PGIN electrodes to induce skin vibration while recording EMG signals. The signal quality was quantified by signal to noise ratio (SNR) (indicates signal clarity), and root-mean-squared (RMS) noise (reflects fluctuations of the signal over time). In static condition, Ag/AgCl showed comparable SNR to PGIN while experienced a sever signal distortion under dynamic condition (Supplementary Fig. S12). This can be attributed to the ultra-conformability of PGIN to maintain consistence contact with skin. In addition, we measured electrocardiogram (ECG), which reflects the health status of heart, both under static and dynamic conditions (Supplementary Fig. S13). In static status, Ag/AgCl and PGIN both captured the characteristic PQRST waveform of ECG. However, for the case of arm swing, Ag/AgCl showed large RMS noise and TP deviation (reflects baseline drift) while PGIN demonstrated good resistance to motion, thereby once again proving the superior conformability of PGIN.

To comprehensively evaluate the performance of PGIN to resist motion artifact, we fabricated a six-channel PGIN electrode array and compared its performance with that of commercial Ag/AgCl electrode. The six-channel electrode array was adhered to the arm and labeled as channel 1 through 6 (ch 1 – ch 6), from the proximal end to the distal end (Fig. 5i). We recorded EMG signals in two conditions: while the arm was static and during arm swings, capturing 10 muscle contractions for each condition. By calculating the SNR extracted from the last muscle contraction in each status, we displayed the spatial SNR performance map for each channel (Fig. 5j, k). In the static status, the SNR for the final muscle contraction measured by both Ag/AgCl and PGIN electrodes maintained > 20 dB, demonstrating excellent recording capability of both types of electrodes. However, under dynamic conditions, the SNR observed with Ag/AgCl electrodes significantly deteriorated, while the SNR for every PGIN channel remained > 20 dB. This difference is mainly due to the way each electrode interfaces with skin. The conformal contact between PGIN electrodes and skin allowed them to move with skin, results in low interfacial impedance, hence maintaining signal quality. Additionally, statistical analysis was used to further access the recording performance of PGIN

electrode. RMS noise changes of the first-time muscle contraction to the last-time contraction static and dynamic conditions were compared between Ag/AgCl and PGIN (Fig. 5l, m). PGIN showed lower RMS noises in both conditions compared to Ag/AgCl, indicating its recording stability under dynamic condition. Moreover, PGIN demonstrated higher SNR values with less variability especially in dynamic conditions, confirming its capability for artifact-free recording. These findings suggest the potential of PGIN as an ultra-conformal bioelectrode for effective and stable electrophysiological sensing and modulating.

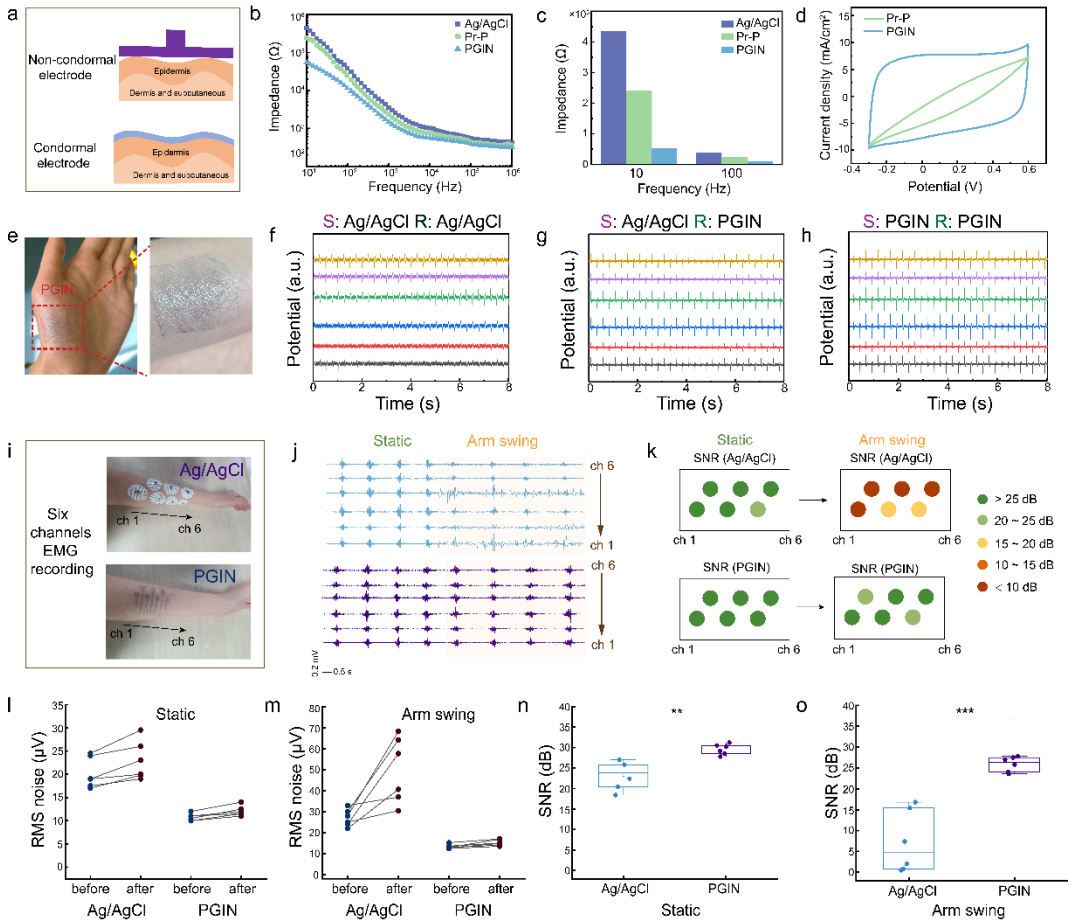

Fig. 5 Electrostimulation and electrophysiological signal detection of PGIN electrode. a Schematic illustration of commercial Ag/AgCl electrode and PGIN electrode on skin. **b** Comparison of interfacial impedance of Pr-P, Ag/AgCl, and PGIN electrodes on skin. **c** Corresponding histograms of impedance values at 10 Hz and 100 Hz. **d** Cyclic voltammetry (CV) curves of Pr-P and PGIN electrodes. **e** A photo of PGIN

adhered to hand as stimulation electrode. **f-h** Multi-channel responses to nerve electrostimulation on the hand with Ag/AgCl as stimulation and recording electrodes (**f**), Ag/AgCl as stimulation electrode and PGIN as recording electrode (**g**), PGIN as stimulation and recording electrodes (**h**). S denotes stimulation and R denotes recording. **i** Photos of multi-channel EMG recording by Ag/AgCl and PGIN electrodes. **j** EMG measured by Ag/AgCl and PGIN electrodes in static and dynamic condition respectively. **k** Spatial SNR performance map for each channel of Ag/AgCl and PGIN for the last muscle contraction in static and dynamic conditions, respectively. **l, m** RMS noise changes of the first-time muscle contraction to the last-time contraction recorded by each of the Ag/AgCl and PGIN channels in static (**l**), and dynamic (**m**) conditions respectively. **n, o** SNR performance of the last muscle contraction recorded by each of the Ag/AgCl and PGIN channels in static (**n**), and dynamic (**o**) conditions respectively. Significance was determined by one-way Anova (*P < 0.05; **P < 0.01; ***P < 0.001; ****P < 0.0001).

Facial EMG (fEMG) monitoring for silent speech recognition

Speaking, as a vital form of communication among humans, plays a crucial role in fostering social connections. However, audible speech may not always be appropriate or possible in certain contexts, such as for individuals with speech impairments, in scenarios requiring privacy, or in environments where silence is necessary[39,40].[39,40] Therefore, silent speech recognition (SSR) technology emerges as a transformative avenue for communication, recording neuromuscular activities on the face during speech and integrating them with machine learning algorithms[41,42].[41,42] SSR hinges critically on the fidelity of facial electromyography (fEMG) signals which requires a high signal quality and presents a significant challenge in practical applications. Traditional approaches to fEMG signal acquisition have predominantly relied on multi-channel commercial electrodes that often suffer from drawbacks such as bulkiness, discomfort, and suboptimal adaptability to facial contours[43,44].[43,44] These limitations can significantly compromise the recognition accuracy and impair the user experience.

Given the diversity of muscle groups on the human face, sensing signals through a single channel bioelectrode is insufficient for high-accuracy speech recognition. By designing ultra-conformal PGIN into multi-channel electrode array, we may capture fEMG signals with high fidelity, thereby achieving reliable silent speech recognition. A six-channel PGIN electrode array was fabricated to cover essential facial areas associated with speech (Fig. 6a). This study engaged eight volunteers who silently read numbers from zero to nine, the numbers were separated by a three second pause, and groupings of ten numbers were ten sets, taking a three-minute break after each set (Fig. 6b). Six-channel Ag/AgCl electrodes were used as comparison (Supplementary Fig. S14). The weak fEMG signals were collected during silent speech using both type of electrodes (Fig, 6c, d). To process these signals for silent speech recognition, we employed two prominent classification algorithms: the support vector machine (SVM) and the convolutional neural network (CNN) deep learning model. Signal segmentation was performed at predetermined intervals. Subsequently, we applied the Short-Time Fourier Transform (STFT) to obtain time-frequency spectral characteristics of each segment (Fig. 6e, f). These characteristics were then fed into classifiers (SVM or CNN) to obtain the final recognition results.

The recognition results for Ag/AgCl and PGIN electrodes, analyzed using SVM and CNN classifiers, are presented in Figures 6g and 6h, respectively. It was observed that the PGIN electrode yielded higher recognition accuracies with both classifiers, achieving up to 92% accuracy (Fig. 6i). This enhanced performance is due to the high SNR provided by PGIN electrodes. Their ultra-conformability to the contours of facial skin and excellent electrochemical properties contribute significantly to this improved SNR. Additionally, CNN architectures outperformed SVM in these SSR experiments. The effectiveness and feasibility of the algorithms were validated by calculating the metrics including Accuracy, Sensitivity, Specificity, Precision, F1 score, Matthews Correlation Coefficient (MCC), and the Kappa score (Fig. 6j, k). Interestingly, we found that the recognition accuracies for words “zero”, “one”, and “two” were lower than

other words (Fig. 6l). This discrepancy is likely due to the unique muscle movements involved in silently speaking these words, which result in fEMG data that are not distinctly separable by the feature extraction process and CNN classifier. This insight suggests the need for further refinement in feature extraction methodologies to enhance recognition accuracy for these specific words. Overall, the high recognition accuracy attained with PGIN electrode array underlines their superiority as ultra-conformal bioelectrodes, particularly in applications that demand high-fidelity signal acquisition.

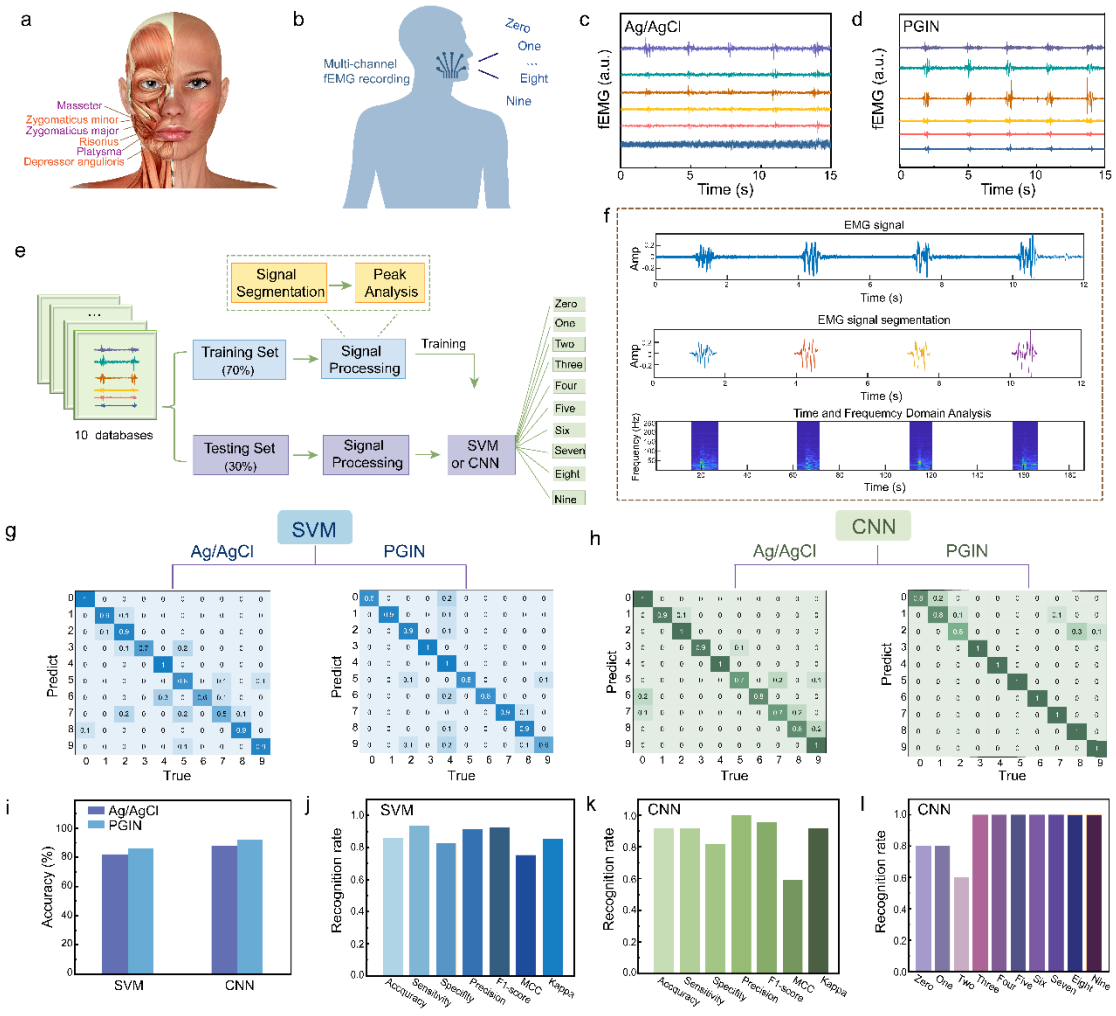

Fig. 6 Facial EMG (fEMG) monitoring for silent speech recognition. a An image showing the main muscles for silent speech analysis. **b** Schematic illustration of six-channel fEMG recording for silent speech recognition. **c, d** Six-channel fEMG recorded by Ag/AgCl (**c**) and PGIN (**d**) electrodes when silently specking number “one”. **e** Flow

chart of the machine learning algorithm for number (0-9) classification. **f** Representative fEMG signals and signal processing steps. **g** Confusion matrix of classification training recognition accuracy of Ag/AgCl and PGIN electrodes by SVM algorithm. **h** Confusion matrix of classification training recognition accuracy of Ag/AgCl and PGIN electrodes by CNN algorithm. **i** Comparison of recognition accuracy of Ag/AgCl and PGIN electrodes by SVM and CNN algorithms. **j, k** Identification results of SVM (**j**) and CNN (**k**). **l** Identification accuracy of each number by PGIN electrode using CNN algorithm.

Discussion

In conclusion, we have successfully developed an ultra-conformal multi-channel bioelectrode array, which consists of PEDOT: PSS and GO interpenetrating network (PGIN). This innovation leverages the exceptional solution processability of both materials, endowing PGIN with design flexibility and simplifying the fabrication process. The synergistic interaction within PGIN results in outstanding opto-electrical conductivity of 2060 S cm^{-1} @ 88% transparency and a mechanical stretchability of up to 110% strain. Moreover, the incorporation of GO significantly enhances the electrochemical performance of the bioelectrode, evidenced by its low interfacial impedance and high charge storage capacity. Taken together its ultrathin feature, it can form a stable interface with skin, achieving effective neuromodulation and artifact-less electrophysiological sensing. Further, by designing PGIN into multi-channel electrode array for fEMG sensing and integrating this with machine learning algorithms, we achieve a high accuracy of 92% in silent speech recognition. Our results show the potential of PGIN in advancing electrophysiological sensing and modulating, pave the way for human-machine interaction.

Methods

Materials. PEDOT: PSS solution (Clevios PH 1000) was purchased from Han Feng; GO aqueous solution was purchased from GaoxiTech; PEGDMA (average Mn 750),

water-soluble initiator 2-Hydroxy-4'-(2-hydroxyethoxy)-2-methylpropiophenone (Irgacure 2959) were purchased from Sigma-Aldrich; sulfuric acid was purchased from Aladdin Industrial Corporation; the SEBS and FS 30 were purchased from Innochem. The tattoo paper was purchased from The Magic Touch Ltd., UK.

Fabrication of PGIN electrode. (i) Preparation of PPIN solution. PPIN solution contains 10 mL PH1000 (solid content ~ 1.3%, PEDOT content ~ 0.37%), PEGDMA was added with 1.4:1 weight ratio vs. PEDOT; 5 wt% of photoinitiator Irgacure 2959 (vs. PEGDMA), and 1 wt% of Capstone™ FS-30 (vs. PH1000). The PPIN solution was then stirred in dark for 5 h. PGIN solution was prepared by adding 3 wt% - 10 wt% GO solution versus PPIN solution and stirred in dark for 5 h. (ii) Patterning of PGIN: PGIN solution was spin-coated on substrate at 1000 r.p.m. for 100 s and dried at room temperature. Later, the PGIN film will undergo photo-crosslinking through exposure to UV light (American Ultraviolet, 25 mW cm^{-2}) using a photomask for 2 min. Following UV exposure, the film will be rinsed with water. As-prepared PGIN film would be further treated with acid by dipping into concentrated sulfuric acid for 10 s followed by rinsing with water and drying. The resulting film, termed as PGIN-S, will then be ready for further testing.

Materials characterization. Surface morphology was observed using an AFM (Nanoscope-III, Digital Instrument). Thickness measurements were carried out with a P7 profilometer from KLA Tencor, America. Raman spectroscopy analysis was conducted using the LabRAM HR Evolution, employing a 532 nm excitation wavelength to examine alterations in the PEDOT structure. To prevent laser-induced local heating, the laser power directed at the sample was maintained below 1 mW. FTIR spectroscopy was collected by SHIMADZU IRTracer 100. Optical transmittance was collected by a SHIMADZU 2450 UV − vis spectrophotometer. Zeta potential was collected by (Malvern)-Zetasizer Nano S90. XPS was performed using an ESCALAB 250Xi spectrometer with monochromatized Al Kα radiation (incident energy, 1486.6eV)

at a pressure of less than 10^{-9} Torr. GIWAXS measurements were conducted with a Xenocs Xeuss 2.0 system, utilizing a copper Xray source. The incident angle applied to the sample was approximately 0.18°. The sample to detector distance is around 17cm. Electrochemical impedance spectroscopy (EIS) analysis was performed with a CHI600e electrochemical workstation from CH Instruments. The sheet resistance was determined using the four-point probe technique with a Keithley 2636b source meter.

Electrophysiological sensing and modulating. (i) For electrophysiological modulating: For electrostimulation of human muscles, two electrodes were applied to the abductor pollicis muscles, serving as the stimulating electrodes. A six-channel electrode array was positioned on the arm to capture the electrostimulation signal through a multi-channel EMG acquisition system. (ii) For electrophysiological signal sensing: a pair of electrodes were placed on forearm, and a reference electrode was placed on the back of wrist. Ag wires and conductive silver paste were used to connect PGIN electrodes to test module. Commercial Ag/AgCl electrodes (3M) were used as reference. To simulate a dynamic status, two methods were employed. First, for single-channel EMG sensing, an electromechanical vibrator was positioned approximately 2 cm from the working electrodes to induce skin vibration. Secondly, to mimic dynamic conditions in both ECG and multi-channel EMG tests, an arm swing action was performed. EMG signals were digitally filtered in MATLAB by a six-order Butterworth filter. (iii) For fEMG measurement, six-channel electrodes were placed on the right side of face to cover the critical areas related to speech, serving as the working electrodes. A ground electrode was placed on the mastoid behind the left ear in accordance with published guidelines[45].[45] Electrodes were connected to test module with Ag wires. Each subject was asked to sit still while 3 min of fEMG signals were recorded as baseline. Then, participants were requested to silently articulate the numbers “zero” through “nine.” These ten numbers were organized into ten sets, with each set consisting of the numbers being silently repeated ten times. A 3 s pause was maintained between each repetition within the sets. After completing a set, participants took a 3-

minute break before proceeding to articulate the next set of numbers. (iv) Silent speech recognition: the collected fEMG data is processed through several stages, including data pre-processing, feature extraction, and classification to attain the recognition rate. The machine learning algorithms used in this study were SVM and CNN.

Note that all the human experiments in this study were approved by the Human Research Ethics Review Committee for Beijing Normal University, and all participants were informed and signed informed consent forms. The ethics number of the experiment is IRB_B_0026 2021001

Reporting summary

Further information on research design is available in the Nature Portfolio Reporting Summary linked to this article.

Data availability

The data that support the findings of this study are provided as source data with this paper or included in the Supplementary Information. Further data are available from the corresponding authors upon request. Source data are provided with this paper.

Code availability

The codes used in this study are available from the corresponding author upon request.

References

1. Lee JM*, et al.* The ultra-thin, minimally invasive surface electrode array NeuroWeb for probing neural activity. *Nat. Commun.* **14**, 7088 (2023).

2. Zhao H*, et al.* Stretchable Multi-Channel Ionotronic Electrodes for In Situ Dual-Modal Monitoring of Muscle–Vascular Activity. *Adv. Funct. Mater.* **34**, 2308686 (2024).

3. Zhou T*, et al.* 3D printable high-performance conducting polymer hydrogel for all-hydrogel bioelectronic interfaces. *Nat. Mater.* **22**, 895-902 (2023).

4. Chen L*, et al.* Dry-Transferable Photoresist Enabled Reliable Conformal Patterning for

Ultrathin Flexible Electronics. *Adv. Mater.* **35**, 2303513 (2023).

5. Lu Y*, et al.* Stretchable graphene–hydrogel interfaces for wearable and implantable bioelectronics. *Nat. Electron.* **7**, 51-65 (2024).

6. Shi X*, et al.* A Sweat Absorbing Skin Electrode for Electrophysiology During Exercise. *Adv. Funct. Mater.* 2314775 (2024).

7. Tian L*, et al.* Large-area MRI-compatible epidermal electronic interfaces for prosthetic control and cognitive monitoring. *Nat. Biomed. Eng.* **3**, 194-205 (2019).

8. Hu W*, et al.* Anisotropic Electronic Skin for Neurofeedback. *Adv. Funct. Mater.* **34**, 2309359 (2024).

9. Jin F*, et al.* Biofeedback electrostimulation for bionic and long-lasting neural modulation. *Nat. Commun.* **13**, 5302 (2022).

10. Gao D, Parida K, Lee PS. Emerging Soft Conductors for Bioelectronic Interfaces. *Adv. Funct. Mater.* **30**, 1907184 (2020).

11. Wu H*, et al.* Materials, Devices, and Systems of On-Skin Electrodes for Electrophysiological Monitoring and Human–Machine Interfaces. *Adv. Sci.* **8**, 2001938 (2021).

12. Song D, et al. An Ultra-Thin MXene Film for Multimodal Sensing of Neuroelectrical Signals with Artifacts Removal. Adv. Mater. 35, 2304956 (2023).

13. Fallegger F, Schiavone G, Lacour SP. Conformable Hybrid Systems for Implantable Bioelectronic Interfaces. *Adv. Mater.* **32**, 1903904 (2020).

14. Xu J, et al. Electrooculography and Tactile Perception Collaborative Interface for 3D Human–Machine Interaction. *ACS Nano* **16**, 6687-6699 (2022).

15. Viana D, et al. Nanoporous graphene-based thin-film microelectrodes for in vivo high-resolution neural recording and stimulation. *Nat. Nanotechnol.* **19**, 514-523 (2024).

16. Luo Y*, et al.* Technology Roadmap for Flexible Sensors. *ACS Nano* **17**, 5211-5295 (2023).

17. Balakrishnan G, Song J, Mou C, Bettinger CJ. Recent Progress in Materials Chemistry to Advance Flexible Bioelectronics in Medicine. *Adv. Mater.* **34**, 2106787 (2022).

18. Du X, Yang L, Liu N. Recent Progress on Poly(3,4-Ethylenedioxythiophene):Poly(Styrenesulfonate) Bioelectrodes. *Small Sci.* **3**, 2300008 (2023).

19. Kayser LV, Lipomi DJ. Stretchable Conductive Polymers and Composites Based on PEDOT

and PEDOT:PSS. *Adv. Mater.* **31**, 1806133 (2019).

20. Yu Z, Xia Y, Du D, Ouyang J. PEDOT:PSS Films with Metallic Conductivity through a Treatment with Common Organic Solutions of Organic Salts and Their Application as a Transparent Electrode of Polymer Solar Cells. *ACS Appl. Mater. Interfaces* **8**, 11629-11638 (2016).

21. Seiti M, Giuri A, Corcione CE, Ferraris E. Advancements in tailoring PEDOT: PSS properties for bioelectronic applications: A comprehensive review. *Biomater. Adv.* **154**, 213655 (2023).

22. Wang Y*, et al.* A highly stretchable, transparent, and conductive polymer. *Sci. Adv.* **3**, e1602076.

23. Tan P*, et al.* Solution-processable, soft, self-adhesive, and conductive polymer composites for soft electronics. *Nat. Commun.* **13**, 358 (2022).

24. Fan X*, et al.* PEDOT:PSS for Flexible and Stretchable Electronics: Modifications, Strategies, and Applications. *Adv. Sci.* **6**, 1900813 (2019).

25. Won D*, et al.* Digital selective transformation and patterning of highly conductive hydrogel bioelectronics by laser-induced phase separation. *Sci. Adv.* **8**, eabo3209.

26. Zheng Y-Q*, et al.* Monolithic optical microlithography of high-density elastic circuits. *Science* **373**, 88-94 (2021).

27. Yang M*, et al.* Robust Neural Interfaces with Photopatternable, Bioadhesive, and Highly Conductive Hydrogels for Stable Chronic Neuromodulation. *ACS Nano* **17**, 885-895 (2023).

28. Jiang Y*, et al.* Topological supramolecular network enabled high-conductivity, stretchable organic bioelectronics. *Science* **375**, 1411-1417 (2022).

29. Zabihipour M*, et al.* High yield manufacturing of fully screen-printed organic electrochemical transistors. *npj Flexible Electron.* **4**, 15 (2020).

30. Lo L-W, Zhao J, Wan H, Wang Y, Chakrabartty S, Wang C. An Inkjet-Printed PEDOT:PSS-Based Stretchable Conductor for Wearable Health Monitoring Device Applications. *ACS Appl. Mater. Interfaces* **13**, 21693-21702 (2021).

31. Du X*, et al.* Transparent and Stretchable Graphene Electrode by Intercalation Doping for Epidermal Electrophysiology. *ACS Appl. Mater. Interfaces* **12**, 56361-56371 (2020).

32. Jang H*, et al.* Graphene e-tattoos for unobstructive ambulatory electrodermal activity sensing on the palm enabled by heterogeneous serpentine ribbons. *Nat. Commun.* **13**, 6604 (2022).

33. Zhao Y*, et al.* Ultra-conformal skin electrodes with synergistically enhanced conductivity for

long-time and low-motion artifact epidermal electrophysiology. *Nat. Commun.* **12**, (2021).

34. Yao B*, et al.* High-stability conducting polymer-based conformal electrodes for bio-/iono-electronics. *Mater. Today* **53**, 84-97 (2022).

35. Tian Y, Yu Z, Cao L, Zhang XL, Sun C, Wang D-W. Graphene oxide: An emerging electromaterial for energy storage and conversion. *J. Energy Chem.* **55**, 323-344 (2021).

36. Gan D*, et al.* Graphene Oxide-Templated Conductive and Redox-Active Nanosheets Incorporated Hydrogels for Adhesive Bioelectronics. *Adv. Funct. Mater.* **30**, 1907678 (2020).

37. Li X*, et al.* Deciphering the superior thermoelectric property of post-treatment-free PEDOT:PSS/IL hybrid by X-ray and neutron scattering characterization. *npj Flexible Electron.* **6**, 6 (2022).

38. Kim S-M*, et al.* Influence of PEDOT:PSS crystallinity and composition on electrochemical transistor performance and long-term stability. *Nat. Commun.* **9**, 3858 (2018).

39. Wang Y*, et al.* All-weather, natural silent speech recognition via machine-learning-assisted tattoo-like electronics. *npj Flexible Electron.* **5**, 20 (2021).

40. Yoo H*, et al.* Silent Speech Recognition with Strain Sensors and Deep Learning Analysis of Directional Facial Muscle Movement. *ACS Appl. Mater. Interfaces* **14**, 54157-54169 (2022).

41. Liu H*, et al.* An epidermal sEMG tattoo-like patch as a new human–machine interface for patients with loss of voice. *Microsyst. Nanoeng.* **6**, 16 (2020).

42. Wu J*, et al.* A novel silent speech recognition approach based on parallel inception convolutional neural network and Mel frequency spectral coefficient. *Front. Neurorobotics* **16**, 971446. (2022).

43. Li W, Yuan J, Zhang L, Cui J, Wang X, Li H. sEMG-based technology for silent voice recognition. *Comput. Biol. Med.* **152**, 106336 (2023).

44. Abdullah A, Chemmangat K. A Computationally Efficient sEMG based Silent Speech Interface using Channel Reduction and Decision Tree based Classification. *Procedia Computer Science* **171**, 120-129 (2020).

45. Fridlund AJ, Cacioppo JT. GUIDELINES FOR HUMAN ELECTROMYOGRAPHIC RESEARCH. *Psychophysiology* **23**, 567-589 (1986).